Design of High Performance CdZnTe Quasi-Hemispherical Gamma-ray CAPture™ Plus Detectors

Derek S. Bale & Csaba Szeles

eV PRODUCTS a division of II-VI, Inc., Saxonburg, PA 16056

ABSTRACT

In this paper we report on the simulation, design, and testing of high performance CdZnTe quasi-hemispherical CAPture™ Plus radiation detectors. Quasi-hemispherical CdZnTe detectors offer a cost effective alternative to other single-polarity (electron-only) detector configurations such as co-planar grid, pixilated or Frish ring CdZnTe detectors with comparable energy resolution both in the high (>500 keV) and low energy range (<500 keV). We have used the device simulation package eVDSIM to design optimal electrode geometry together with the necessary material selection criteria for charge transport properties of the CdZnTe crystals. A test set of 10x10x5mm^3 CAPture™ Plus detectors has been built using state-of-the art fabrication technology. The measured spectral and efficiency performance of these detectors is compared to the theoretical predictions of simulation. Our results demonstrate that with careful selection of uniform material and high-quality fabrication, this design of CAPture™ Plus detectors is capable of regularly achieving FWHM @ 81keV of 5%, FWHM @ 122keV of <3%, and FWHM @ 662keV of <2%.

Keywords: Cadmium Zinc Telluride, CdZnTe, nuclear radiation detectors, quasi-hemispherical detectors, x-ray and γ-ray spectroscopy

1. INTRODUCTION

The physical properties of semi-insulating Cadmium Zinc Telluride (CdZnTe) such as high atomic number, high density, wide band gap, low chemical reactivity and long term stability make it an excellent material candidate for high efficiency, high-resolution room-temperature nuclear radiation detectors. Intense research of crystal growth and electrical compensation in CdZnTe in the last 10-15 years has led to the developments that allow the growth of CdZnTe crystals with low defect density and very good charge transport properties. Today, CdZnTe crystals are available commercially and CdZnTe based room-temperature radiation detectors and detector arrays are steadily gaining acceptance in many medical, industrial, security, safeguards and scientific X-ray and γ-ray imaging and spectroscopic applications.[1]

While CdZnTe crystals are readily available for simpler counting and monitoring applications, large field-of-view imaging and high-sensitivity, high-resolution spectroscopic applications demand larger and more uniform CdZnTe single crystals with better charge transport properties. The electron mobility-lifetime product ($\mu\tau_e$) of CdZnTe crystals grown by the high-pressure electro-dynamic gradient freeze (HP EDGF)[2], conventional vertical Bridgman[3] and traveling heater method (THM)[4] have steadily climbed from the low 10^{-3} cm^2/V range to the 10^{-2} cm^2/V $\mu\tau_e$ range in recent years. On the other hand, the growth of CdZnTe *single crystals*, with spatially uniform charge transport properties that are required for these applications remains a huge challenge due to the inherent complexity of the crystallization and defect formation processes in these crystals.[5,6]

High performance spectroscopic CdZnTe detectors such as the 3D depth sensing position sensitive devices (3D DSPS)[7], and co-planar grid detectors (CPG)[8] require the highest electron transport and uniformity single crystals to achieve the best possible energy resolution. In addition, the readout electronics and integration cost of these devices is relatively high. In particular the 3D DSPS detector applications require 100+ readout channels and significant computational overhead to perform the depth and multiple-interaction corrections. Because of the high manufacturing costs, it is not logical to fabricate 3D DSPS and CPG detectors from lower quality CdZnTe crystals. In contrast, Frisch ring[9,10] and quasi-hemispherical[11] devices require only a single readout channel and can potentially be produced at a lower cost with only modest performance tradeoff. Therefore, it is important to develop an understanding of the performance and fabrication cost tradeoffs for these simple detector configurations, and develop the CdZnTe crystal performance requirements to achieve a given target performance.

Hard X-Ray and Gamma-Ray Detector Physics VIII, edited by Larry A. Franks, Arnold Burger, Ralph B. James, Proceedings of SPIE Vol. 6319 (SPIE, Bellingham, WA, 2006)

In this paper, we analyze the dependence of the spectral performance of quasi-hemispherical CAPture™ Plus detectors on relevant detector design parameters. We have used the device simulation package eVDSIM (**eV** PRODUCTS **D**evice **SIM**ulation package) to develop an understanding of the influence on performance of such design parameters as the pixel diameter, bias voltage, and the free carrier mobility-lifetime products of the CdZnTe crystal. This information has been used to develop a material selection and prototype fabrication process aimed at producing high-performance spectroscopic detectors with high yield and low manufacturing cost.[12]

In the following sections we begin by briefly introducing the structure, capabilities and configuration of eVDSIM. Next we present examples for which eVDSIM has been used to explore the electrostatic and weighting fields within quasi-hemispherical detectors. Following this discussion, the dependence of charge collection on quasi-hemispherical design parameters is investigated. Finally, we validate the predictions provided by simulation with experimental measurements.

2. DETECTOR DESIGN & SIMULATION WITH EVDSIM

A typical CdZnTe quasi-hemispherical CAPture™ Plus detector is shown in Fig. 1. The essential design parameters for this detector configuration are the physical dimensions (*X*, *Y*, *Z*), the pixel diameter (*d*), bias voltage (*V*), and the electron and hole mobility-lifetime products ($\mu\tau_e$ and $\mu\tau_h$), respectively. The quasi-hemispherical design[1,2] sets the length- and width-to-thickness ratios (i.e. $X/Z = Y/Z = 2$). The choice of the detector thickness (Z) is driven by the photon energy range of interest and desired detection efficiency. The dependence of detector performance on the remaining design parameters {d, V, $\mu\tau_e$, $\mu\tau_h$} is non-trivial and must be investigated numerically. Therefore, we have used the device simulation package eVDSIM to perform a large set of numerical simulations aimed at understanding the nature of the influence that the pixel diameter, bias voltage, and free carrier mobility-lifetime products have on detector performance. The results of these simulations will be presented in the following sections.

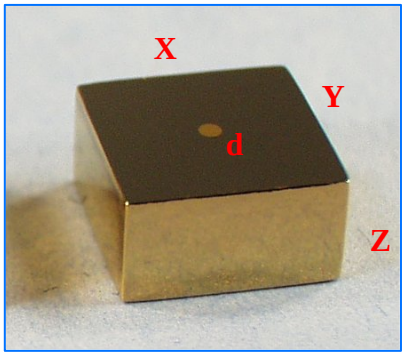

Fig. 1. Quasi-hemispherical CdZnTe detector configuration.

eVDSIM is a multi-platform (i.e. Linux and Windows) library of C/C++ classes and routines developed at eV PRODUCTS for the simulation of semi-insulating CdZnTe radiation detectors. It provides the necessary tools for engineering design of a wide variety of detector configurations by allowing for arbitrary two- and three-dimensional electrode geometries, and surface charge conditions. The electrostatic and weighting fields are computed using both relaxation and multi-grid techniques. Photon transport algorithms are based on Monte Carlo techniques, and make use of analytical interaction cross sections derived by J. Baro et. al.[13]

Much of the flexibility offered by eVDSIM is derived from the use of polymorphism within its object-oriented design. That is, high-level classes often make use of lower-level class libraries that define re-usable functionality for geometric shapes, grid functions, and other objects. The setup and configuration of a simulation within eVDSIM is modeled after a typical radiation detector test bench that includes a source, detector, shaping electronics and a multi-channel analyzer. The classes within eVDSIM that emulate such an experimental setup are shown in Fig. 2. A detector object is first configured by defining both the CdZnTe material, and detector electrode geometry. One then defines a device by adding objects that provide the functionality of a radiation source and the pulse processing electronics. Once the device object is configured and instantiated, library routines that utilize the device object can be

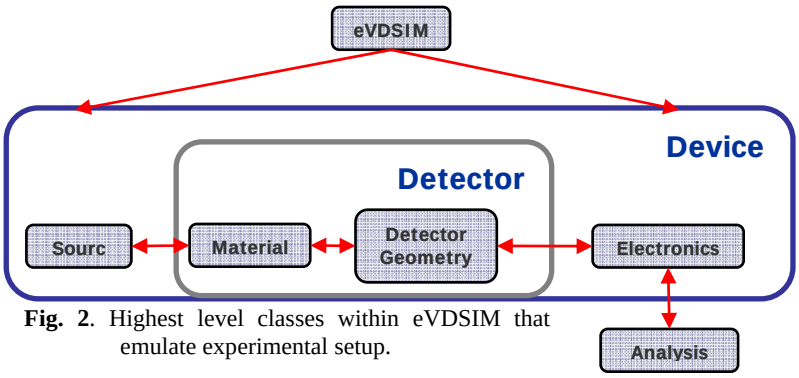

Fig. 2. Highest level classes within eVDSIM that emulate experimental setup.

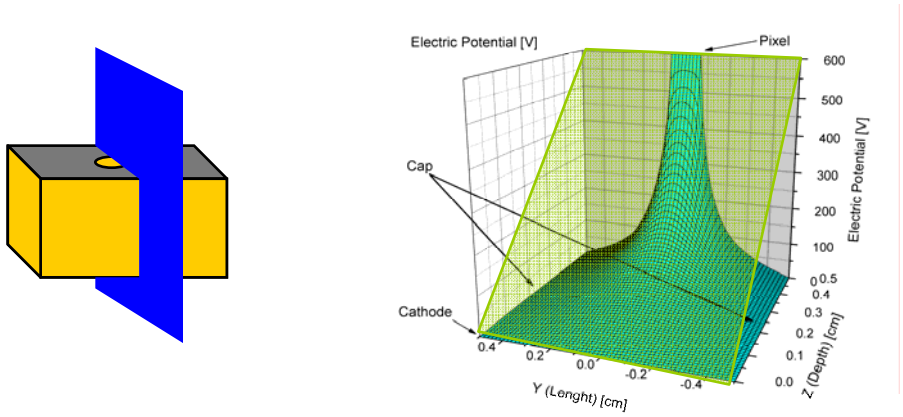

Fig. 3. (left) Quasi-hemispherical detector with 2D plane cut through the center of the pixel. (right) The electric potential [V] within the 2D plane is shown as a mesh plot. The electric potential of a planar detector at the same bias voltage is also shown.

implemented to compute electrostatic and weighting fields, and generate charge induction maps and energy spectra. Finally, analysis routines are available to provide detailed information about design criteria such as peak resolution, detector efficiency, or any other quantity of interest.

3. ELECTROSTATIC & WEIGHTING FIELDS

The charge collection performance of semiconductor radiation detectors depends critically on both the electrostatic and weighting fields within the detector volume. It follows that a key step in the investigation of the performance of the quasi-hemispherical CAPture™ Plus detector is an understanding of the electric and weighting potentials that result due to the application of a positive bias voltage to the detector pixel.

The left pane of Fig. 3 shows the basic two-terminal structure of the quasi-hemispherical design – a five-sided cathode together with a small pixel on the anode plane. The right pane of Fig. 3 shows a mesh plot of a 2D slice of the electric potential that results due to the application of a 600 volt bias. The particular slice being shown is through the center of the pixel as indicated in the left pane of the figure. Also shown in the right pane of Fig. 3 is the resulting electric potential due to the same bias voltage in a planar detector. It is immediately clear from this plot that the effect of

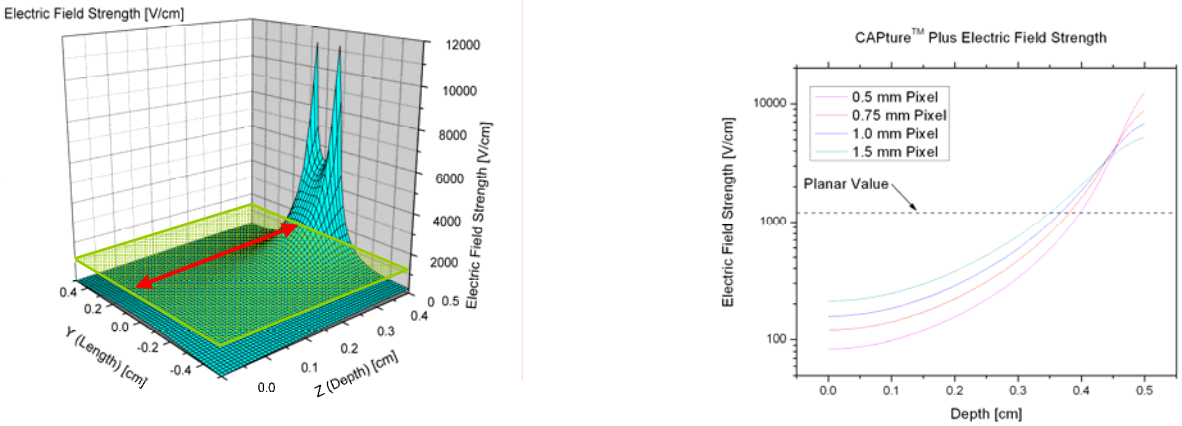

Fig. 4. (left) Mesh plot of the electric field strength within the 2D slice through the detector volume. The strength of the electric field within an equivalently biased planar detector is also shown as a uniform plane. (right) The field strength along the center line of the pixel due to various pixel sizes.

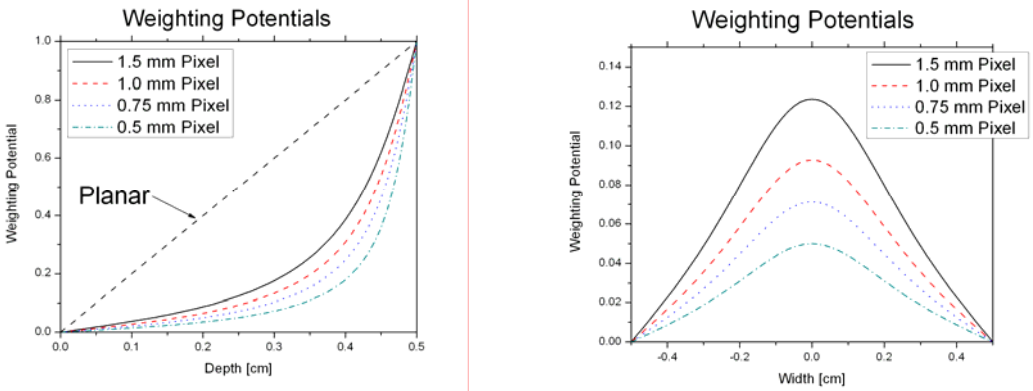

Fig. 5. (left) Quasi-hemispherical weighting potential along center line of the pixel at various pixel sizes. (right) Weighting potential along a line perpendicular to the centerline at a depth of 0.25 cm for same set of pixel sizes.

the quasi-hemispherical electrode geometry is a reduced electric potential throughout the detector volume when compared to that of a planar detector. This is mainly due to the fact that all five sides of the cathode remain at the same potential, thereby pinning the potential at the detector boundaries and forcing a non-linear potential distribution.

The electric field strength that results due to the non-linear potential distribution is shown as a mesh plot in the left pane of Fig. 4 for the same 2D slice through the detector volume. For comparison, we also show the field strength of an equivalently biased planar detector, which is simply a uniform field throughout the slice. Note that the field strength within the quasi-hemispherical detector is lower than that of the planar detector throughout most of the detector volume. In fact, the right pane of Fig. 4 shows the field strength down the center line of the pixel (red arrows in left pane) for various pixel sizes. We point out that even though this centerline is a local maximum of the field strength, the values along this line are significantly smaller than those of the equivalently biased planar detector (straight dashed line in right pane of Fig. 4).

Though the reduced electric field strength will locally slow free carriers down and increase trapping probabilities, the benefit of the quasi-hemispherical design is greatly improved charge collection. The improvement in charge collection is due to a suppression of the weighting potential as seen in Fig. 5. The left pane of this figure shows the weighting potential down the centerline of the pixel for the same set of pixel diameters as was shown in the right pane of Fig. 4. Also shown is this plot is the weighting potential of a planar detector with the same size (dashed line). The right pane of Fig. 5 shows the same potential along a line perpendicular to the centerline, and at a depth of 2.5 mm. The suppressed weighting potential of the quasi-hemispherical electrode geometry heavily weights the dependence of

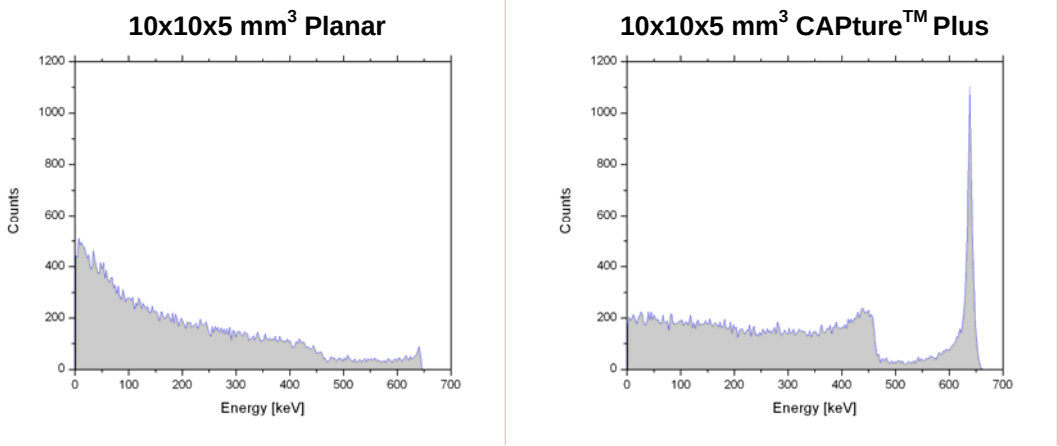

Fig. 6. (left) Simulated ^{137}Cs spectrum for a 10x10x5 mm^3 planar detector under 600 V bias. (right) Simulated ^{137}Cs spectrum for a 10x10x5 mm^3 quasi-hemispherical CAPture™ Plus detector.

charge induction away from the hole transport, and towards a more efficient free electron induction.

The reduced electric field strength in the quasi-hemispherical design is simply the price one has to pay for the significant improvement in charge collection. In fact, this is a necessary truth for any two-terminal detector design due to the fact that the weighting potential is functionally equivalent to the electric potential up to a scaling factor. The simulated spectra in Fig. 6 where generated by exposing a planar (left pane) and CAPture^{TM} Plus detector (right pane) to a ^{137}Cs source for the same amount of time. These spectra demonstrate the improved charge collection due to the quasi-hemispherical design for a 10x10x5 mm^3 CdZnTe crystal under 600 V bias, with $\mu\tau_e$=7x10^{-3} cm^2/V and $\mu\tau_h$=5x10^{-5} cm^2/V. The left pane of Fig. 6 shows a weak 662 keV peak in the simulated planar spectrum, while the right pane shows a very sharp peak produced by the quasi-hemispherical CAPture^{TM} Plus detector. Both the peak resolution and photo-peak efficiency of the quasi-hemispherical design are clearly superior to that of the planar, resulting in a drastically improved peak-to-Compton ratio. It is also important to note that the integrated counts in both spectra of Fig. 6 are the same (within statistical fluctuations). Since both detectors were exposed to the same source for the same amount of time, we conclude that for these particular design parameters the CAPture^{TM} Plus detector has a fully active volume relative to the Planar detector. This is due to the fact that although the electric field is lower throughout most of the detector, the electrons experience a large acceleration in the near pixel region so that their total time of flight is comparable to the planar time of flight.

4.CHARGE INDUCTION

We now present a selection of results from a large set of simulated data generated using eVDSIM. Our focus will be on understanding the affect that each of the design parameters have on charge collection, and therefore spectral quality, within the CAPture^{TM} Plus detector. The primary tool we use for this task is the charge induction map shown in the right pane of Fig. 7. Each point in this map represents an event that deposited energy within the detector, and quantifies the fraction of induced charge (y-axis) as a function of the depth of deposition (x-axis) for that event. The color (shading) of each point indicates the lateral distance away from the centerline of the pixel that the event took place. Red points indicate deposition along the centerline, while blue points indicate deposition near the edge of the

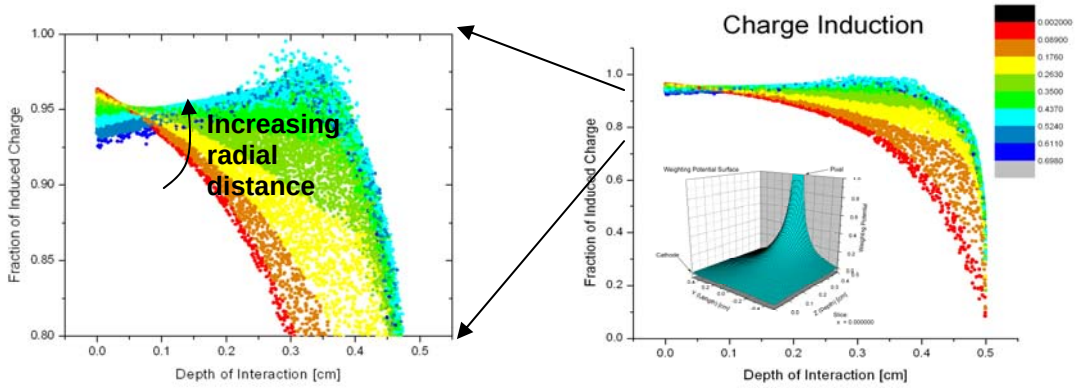

Fig. 7. (right) Charge induction map for a quasi-hemispherical detector. The x-axis is the depth of interaction measured in cm, and the y-axis is the fraction of charge that is induced. The inset is a mesh plot of the weighting potential. (left) A blow-up plot of the peak-forming region of the induction map. Increasing radial distance from the pixel center line is indicated by the arrow.

detector.

The resulting energy spectrum from all events for a mono-energetic source is simply a projection of the points in Fig. 7 onto the y-axis, and a delta-function peak would be represented by a horizontal line. That is, a horizontal line indicates that the charge induction is independent of the depth of interaction. The plot on the left pane of Fig. 7 focuses in on the peak-forming region of the induction map. The arrow in this plot indicates the direction of increasing lateral distance (i.e. red to blue). Finally, it is useful to note that positive slopes in these plots imply an increase in the induced fraction with increasing depth of deposition, meaning that the induction process is limited by the trapping of electrons.

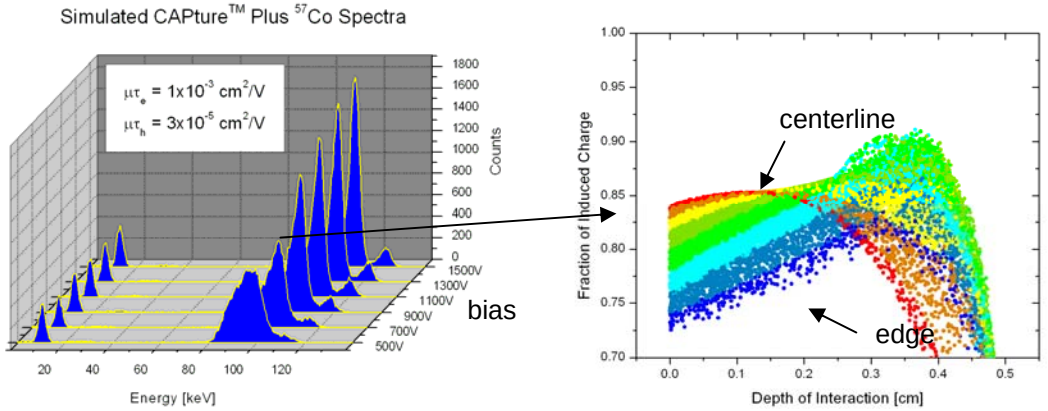

Fig. 8. (left) Simulated ^{57}Co spectra for a 10x10x5 mm^3 CAPture™ Plus detector at various bias voltages. (right) Charge induction map for the spectrum simulated at a 700 V bias.

However, negative slopes imply a decrease in the induced fraction with increasing depth of deposition. This indicates that the induction process is limited by the weighting potential (i.e. the electrode geometry).

We discussed in the previous section that the electric field throughout most of the volume of a quasi-hemispherical detector is lower than that of an equivalent planar detector under the same bias. The ramifications of the reduced electric field for material with low electron transport can be seen in Figs. 8 & 9. The left pane of Fig. 8 shows the simulated ^{57}Co spectral response of a 10x10x5 mm^3 CAPture™ Plus detector with a 1mm pixel at bias voltages between 500 V and 1500 V. The CdZnTe crystal was chosen to have low electron transport with $\mu\tau_e$=1x10^{-3} cm^2/V, and hole transport with $\mu\tau_h$=3x10^{-5} cm^2/V. Note that the peak resolution at high bias is very good, but the quality degrades below 1000 V. The induction map for the 700 volt simulation is shown in the right pane of Fig. 8. The reduced gain and positive slopes in this map indicate that the poor spectral quality is due to excessive electron trapping.

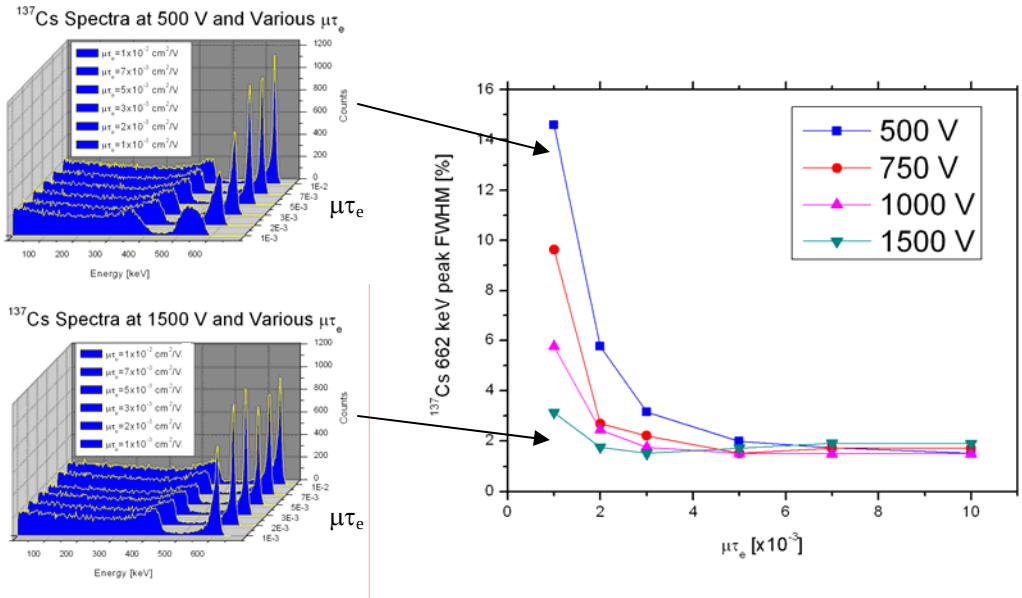

Fig. 9. Peak resolution (FWHM) at 662 keV for a 10x10x5 mm^3 CAPture™ Plus detector. Electron mobility-lifetime products are between 1x10^{-3} cm^2/V and 1x10^{-2} cm^2/V, and bias voltage is between 500 and 1500 volts. Spectra are shown at 500 V and 1500 V for all $\mu\tau_e$

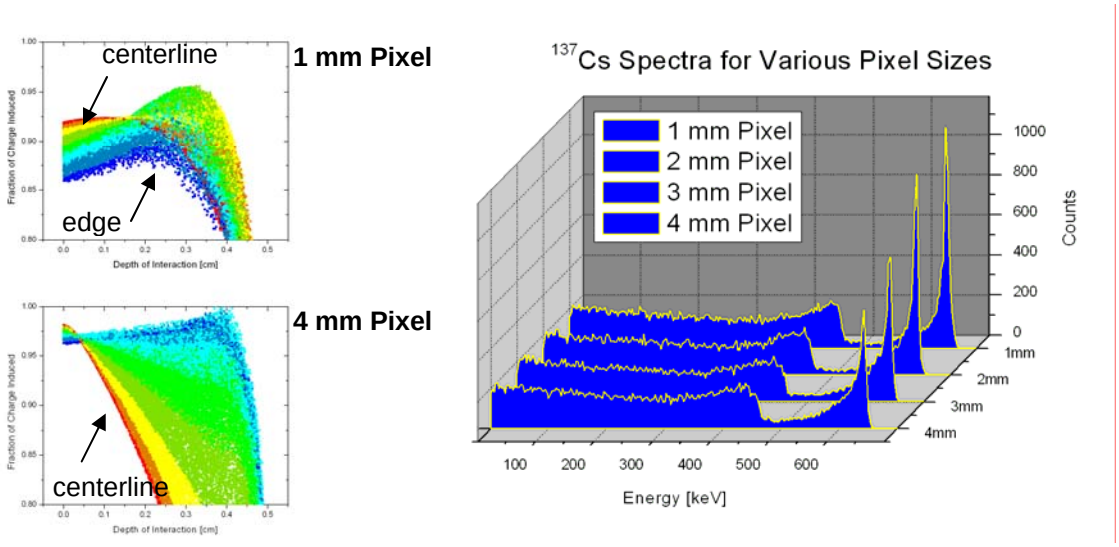

Fig. 10. ^{137}Cs spectral performance for 10x10x5 mm^3 quasi-hemispherical designs with varying pixel size. The induction map on the top left is for a 1 mm pixel, while the induction map on the bottom left is for a 4 mm pixel.

A similar study for ^{137}Cs spectra is summarized in Fig. 9, however, in the simulations presented in this figure we have also varied the electron mobility-lifetime product between $\mu\tau_e=1x10^{-3}$ cm^2/V and $\mu\tau_e=1x10^{-2}$ cm^2/V. The plot in the right pane of Fig. 9 shows that if $\mu\tau_e>4x10^{-3}$ cm^2/V, the quasi-hemispherical detector is expected to achieve resolution better than 2% FWHM at 662 keV for all voltages between 500 V and 1500 V. However, for $\mu\tau_e<4x10^{-3}$ cm^2/V the dependence of resolution on the bias voltage is very strong. These results demonstrate that the spectral performance of quasi-hemispherical detector depends strongly on both the electron mobility-lifetime product and the bias voltage.

It is also interesting to study the influence that the pixel diameter has on charge induction. Fig. 10 summarizes the results of simulating a set of 10x10x5 mm^3 CAPture^{TM} Plus detectors biased at 1000 V with pixel diameters d = {1, 2, 3, 4} mm subjected to a ^{137}Cs source. The CdZnTe crystals were chosen to have $\mu\tau_e=7x10^{-3}$ cm^2/V and $\mu\tau_h=3x10^{-5}$ cm^2/V. The plot of spectra on the right shows an increased amount of tailing as the pixel size is increased. This is confirmed by noting that the FWHM at 662 keV for the 1mm pixel is 1.7%, while the FWHM for the 4mm pixel is 2.5%, but the FWTM for these pixel sizes are 5.4% and 14%, respectively.

The induction maps in Fig. 10 make clear what is driving the increased tailing. Recall that the red points represent interactions along the pixel centerline, while blue points are interactions near the edge of the detector. The map for the 1mm pixel is on the top left and shows that the low field of the smaller 1mm pixel reduces induction for edge events, while the suppressed weighting potential increases the induction of centerline interactions. This results in a fairly uniform induced fraction throughout the depth of the detector and produces good peak resolution. The 4mm pixel, on the other hand, produces a stronger electric field that reduces the electron trapping as seen by the higher gain and lower slope of the edge interactions. At the same time the increased weighting potential reduces the induction of centerline events as indicated by the large negative slope. The result is fanned out non-uniform induction map that is skewed, which produces a larger low energy tail.

Finally, we consider the affect that hole transport has on the detector performance. Once again we have simulated a 10x10x5 mm^3 CAPture^{TM} Plus detector at 1000 V bias and exposed to both ^{57}Co and ^{137}Cs sources. The electron transport was set to $\mu\tau_e=7x10^{-3}$ cm^2/V, and the hole transport was varied over two orders of magnitude, from $\mu\tau_h=3x10^{-6}$ cm^2/V to $\mu\tau_h=3x10^{-4}$ cm^2/V. Fig. 11 shows the spectral responses of the detectors for both sources at the two extreme hole mobility-lifetime products. The induction map for $\mu\tau_h=3x10^{-6}$ cm^2/V is shown in the top left pane, and the map for $\mu\tau_h=3x10^{-4}$ cm^2/V in the lower left pane. Most note worthy within the induction maps is the fact that events near the edge of the detector induce exactly the same fraction of charge for hole transport that ranges over two orders of magnitude. This is expected due to the fact that the weighting potential vanishes near the edge of a quasi-hemispherical

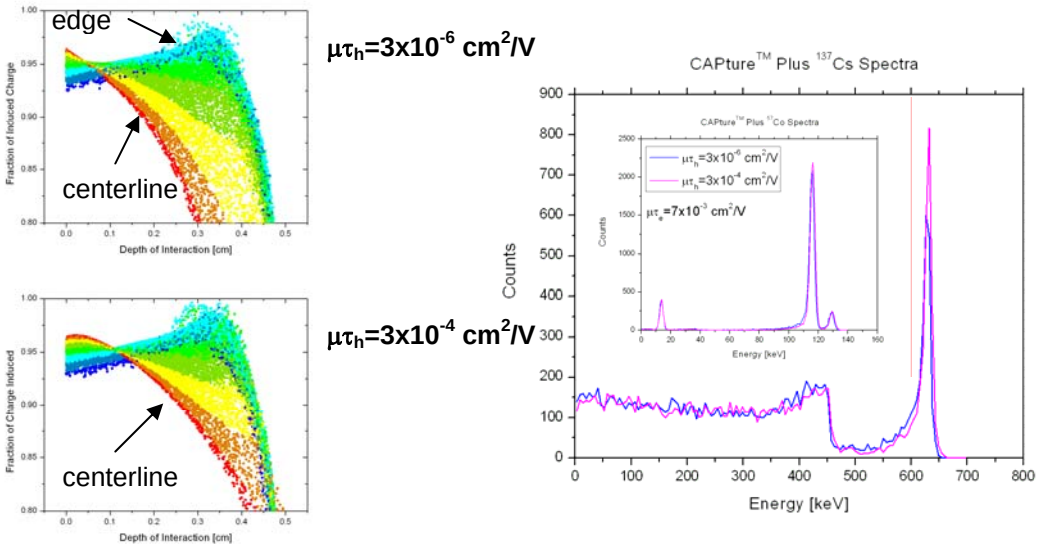

Fig. 11. Comparison of ^{57}Co (inset plot on right) and ^{137}Cs spectra for a 10x10x5 mm^3 quasi-hemispherical detector with both low hole transport ($\mu\tau_h$=3x10^{-6} cm^2/V) and high hole transport ($\mu\tau_h$=3x10^{-4} cm^2/V). The induction map on the top left is for low hole transport, and the map on the lower left is for high hole transport.

detector. Down the centerline, however, there is a slight improvement in the charge induction for the higher hole transport material. As indicated by the resulting spectra, however, it is only a modest improvement.

The simulation data generated by eVDSIM has clearly distinguished the electron transport of the CdZnTe crystal ($\mu\tau_e$) together with the bias voltage from both the hole transport ($\mu\tau_h$) and pixel diameter (d) as dominant design parameters. The data demonstrates that the strong dependence of the detector performance on electron transport and bias voltage as indicated in Figs. 8 & 9 must be taken into account when designing quasi-hemispherical CAPture™ Plus detectors. At the same time, the pixel diameter and hole transport of the crystal do affect performance, but they can only be used as second-order performance tuning parameters.

COMPARISON WITH FABRICATED DETECTORS

The insight gained through simulation into the dependence of detector performance on the set of design parameters {d, V, $\mu\tau_e$, $\mu\tau_h$ } has been used to develop a material selection and fabrication process for these detectors. This process, together with an overview of CdZnTe crystal growth, mining and characterization at eV PRODUCTS is described in a paper by C. Szeles, D.S. Bale, J. Grosholz, G.L. Smith, M. Blostein and J. Eger in these proceedings.[12] In order to validate the theoretically predicted performance discussed in the previous sections, we have fabricated a significant quantity of 10x10x5 mm^3 quasi-hemispherical CAPture™ Plus detectors according to the process described in [12]. Spectra have been taken for ^{133}Ba, ^{57}Co and ^{137}Cs sources with an applied bias of 1500 V, a shaping time of 1 μs, and utilizing the eV-550 preamplifier. Fig. 12 shows a comparison between measured (left) and simulated (right) ^{57}Co and ^{137}Cs spectra shown together and normalized. Comparison of the peak shapes is reasonably good. Note that no attempt has been made to match the gain of the measured spectrum to that of the simulation.

Prior to the CAPture™ Plus fabrication step, these detectors where fabricated as planar detectors, and $\mu\tau_e$ was measured by fitting the voltage dependence of the 5.5 MeV photopeak from a ^{241}Am alpha source to the Hecht model.[14] Knowing $\mu\tau_e$ of the fabricated detectors allows us to directly compare the measured and simulated spectral performance at multiple bias voltages. In Fig. 13, we compare measured and simulated FWHM peak resolution for both ^{57}Co (left pane) and ^{137}Cs (right pane) sources at bias voltages between 400 V and 1600 V. The fabricated detector had a measured $\mu\tau_e$=7.6x10^{-3} cm^2/V. Blue triangles represent the measured data, while red squares represent the simulated data. Comparison is good for high bias voltages, particularly for the ^{137}Cs peak at 662 keV. The high values predicted by simulation for the FWHM at high bias voltages for the ^{57}Co peak at 122 keV is due to an over-estimation of the

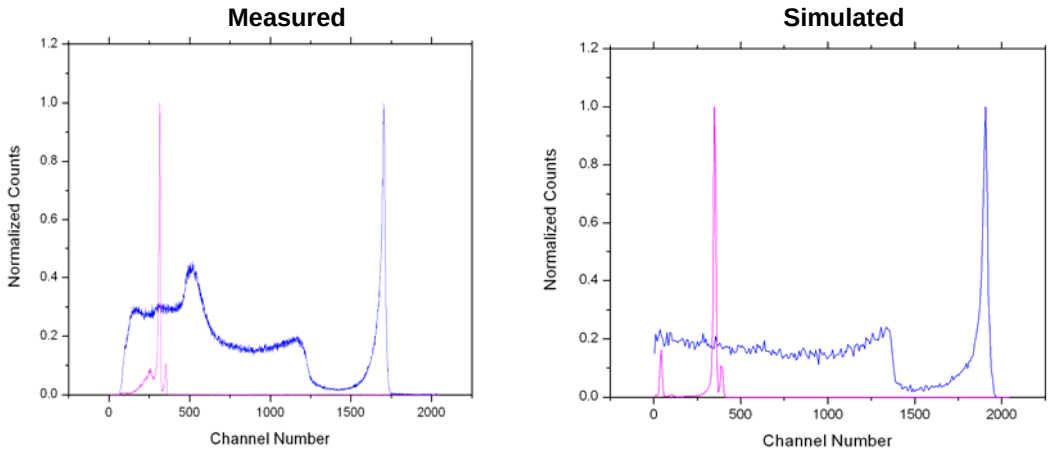

Fig. 12. Comparison of measured (left) and simulated (right) ^{57}Co and ^{137}Cs spectra.

electronic noise. In addition, the deviation of the FWHM at low bias voltages for both sources is likely due to charge collection non-uniformities discussed in [12].

Finally, Fig. 14 shows the FWHM peak resolution for ^{137}Cs of the set of fabricated detectors (blue triangles), together with simulated curves at four bias voltages between 500 V and 1500 V. As one may expect, the better-performing fabricated detectors perform at, or near, the FWHM predicted by simulation. However, there does exist a significant scatter in the measured data at any given $\mu\tau_e$. Based on earlier studies of performance deterioration for both 3D DSPS and CPG detectors, we suspect that the energy resolution deviations of quasi-hemispherical devices is also caused by Te inclusions in the crystals. We discuss this topic in more detail in [12].

6. CONCLUSIONS

In this study we have used the simulation package eVDSIM to numerically investigate the dependence of the performance of quasi-hemispherical CAPture^{TM} Plus detectors on design parameters such as the pixel diameter, bias voltage, and the free carrier mobility-lifetime products (i.e. {d, V, $\mu\tau_e$, $\mu\tau_h$}). We have demonstrated that the non-linear

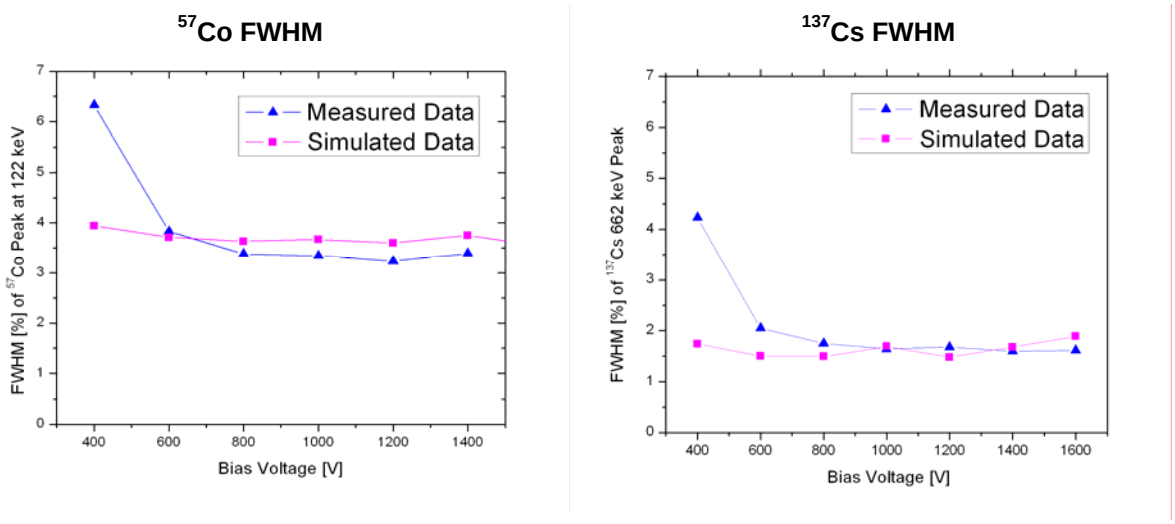

Fig. 13. Comparison of measured (triangles) and simulated (squares) FWHM peak resolutions for ^{57}Co (left pane) and ^{137}Cs (right pane) sources.

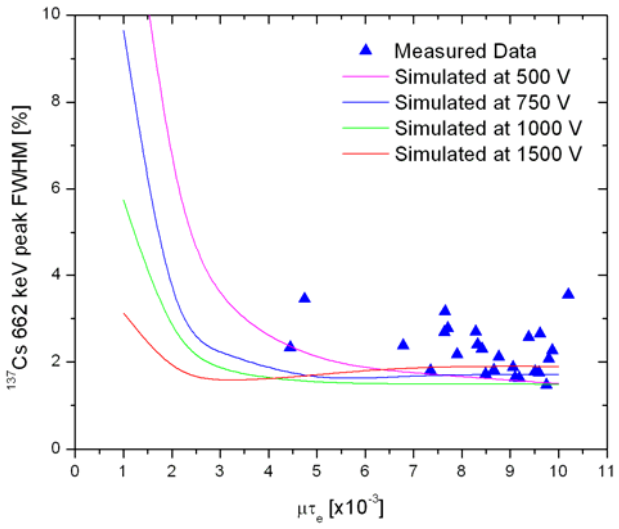

Fig. 14. Comparison of the FWHM at 662 keV for the set of fabricated CAPture™ Plus detectors (blue triangles) and the resolution predicted by simulation (solid curves) for four different bias voltages between 500 V and 1500 V.

electric potential distribution results in a detector performance that predominantly depends on the electron mobility-lifetime product ($\mu\tau_e$) of the CdZnTe crystal, as well as the applied bias voltage (V). It was also demonstrated that the hole mobility-lifetime product ($\mu\tau_h$), and the pixel diameter (d) affect detector performance, but to a lesser degree. The simulation data have been used to develop both material selection and design criteria for CAPture™ Plus detectors aimed at improving test yields and thereby lowering manufacturing costs.

A significant number of CAPture™ Plus detectors have been fabricated using the new material selection and design criteria. These detectors have been tested, and the results were compared to simulation data. It was found that the experimental data from the better-performing detectors compared well with simulation. However, there is scatter in the experimental data that indicates the presence of charge collection non-uniformities in the CdZnTe crystals that we studied. This topic is currently under investigation, and will be reported on in future publications.

REFERENCES

[1] T.E. Schlesinger, J.E. Toney, H. Yoon, E.Y. Lee, B.A. Brunett, L. Franks, and R.B. James, *Mater. Sci. Eng.* **R32**, 103 (2001).

[2] Cs. Szeles, S.E. Cameron, S.A. Soldner, J.-O. Ndap, M.D. Reed, *J. Electron Mater.* **33**, 742 (2004).

[3] L. Li, F. Lu, C. Lee, G.W. Wright, D.R. Rhiger, S. Sen, K.S. Shah, M.R. Squillante, L.J. Cirignano, R.B. James, A. Burger, P.N. Luke, R. Olsen, *SPIE Proceedings Series*, Vol. **4787**, 76 (2003).

[4] Redlen Crystals (private communication).

[5] Cs. Szeles, W.C. Chalmers, S.C. Cameron, J.-O. Ndap, M. Bliss, and K.G. Lynn, *SPIE Proceedings Series*, Vol. **4507**, 57 (2001).

[6] M. Fiederle, V. Babentsov, J. Franc, A. Fauler, and J.-P. Konrath, *Cryst. Res. Technol.* **38**, 588 (2003).

[7] F. Zhang, Z. He D. Xu, G.F. Knoll, D.K. Wehe, J.E. Berry, *IEEE Trans Nucl. Sci.* **NS-51**, 2427 (2004).

[8] M. Amman, J.S. Lee, and P.N. Luke, *J. Appl. Phys.* **92**, 3198 (2002).

[9] D.S. McGregor, Z. He, H.A. Seifert, D.K. Wehe, R.A. Rojeski, Appl. Phys. Lett., Vol. **72**, No. 7, (1998)

[10] W.J. McNeil, D.S. McGregor, A.E. Bolotnikov, G.W. Wright, R.B. James, Appl. Phys. Lett. Vol **84**, No. 11 (2004)

[11] V. Ivonov, P. Dorogov, *Proc. ESARDA 19th Annual Symposium on Safeguards and Nuclear Material Management* (1997). V. Ivanov, P. Dorogov, A. Loutchansky, L. Aleksejeva, E. Mozaev, *Proc. ESARDA Symposium on Safeguards and Nuclear Material Management* (1999).

[12] C. Szeles, D.S. Bale, J. Grosholz, G.L. Smith, M. Blostein, J. Eger, these proceedings (6319A-10).

[13] J. Baro, M. Roteta, J.M. Fernandez-Varea and F. Salvat, *Radiat. Phys. Chem.*, Vol. **44** No. 5, *531* (1994).

[14] K. Hecht, *Zeits. Phys.* **77**, 235 (1932).